

Article

Impact of Oxygen Vacancy on the Photo-Electrical Properties of In₂O₃-Based Thin-Film Transistor by Doping Ga

Kuan-Yu Chen ^{1,2}, Chih-Chiang Yang ^{2,*}, Yan-Kuin Su ^{1,2,*}, Zi-Hao Wang ³ and Hsin-Chieh Yu ^{3,4}

¹ Department of Electrical Engineering, Institute of Microelectronics, National Cheng Kung University, Tainan 701, Taiwan; cncr7025@gmail.com

² Green Energy Technology Research Center, Department of Electrical Engineering, Kun Shan University, Tainan 710, Taiwan

³ Advanced Optoelectronic Technology Center, National Cheng Kung University, Tainan 701, Taiwan; kmurder1118@gmail.com (Z.-H.W.); hcyu@nctu.edu.tw (H.-C.Y.)

⁴ College of Photonics, Institute of Lighting and Energy Photonics, National Chiao Tung University, Tainan 711, Taiwan

* Correspondence: 298r.yang@gmail.com (C.-C.Y.); yksu@mail.ncku.edu.tw (Y.-K.S.); Tel.: +886-6-275-7575 (ext. 62400-1216) (C.-C.Y.); +886-6-275-7575 (ext. 62382) (Y.-K.S.)

Received: 29 January 2019; Accepted: 23 February 2019; Published: 4 March 2019



Abstract: In this study, amorphous indium gallium oxide thin-film transistors (IGO TFTs) were fabricated by co-sputtering. Three samples with different deposition powers of the In₂O₃ target, namely, sample A with 50 W deposition power, sample B with 60 W deposition power, and sample C with 70 W deposition power, were investigated. The device performance revealed that oxygen vacancies are strongly dependent on indium content. However, when the deposition power of the In₂O₃ target increased, the number of oxygen vacancies, which act as charge carriers to improve the device performance, increased. The best performance was recorded at a threshold voltage of 1.1 V, on-off current ratio of 4.5×10^6 , and subthreshold swing of 3.82 V/dec in sample B. Meanwhile, the optical properties of sample B included a responsivity of 0.16 A/W and excellent ultraviolet-to-visible rejection ratio of 8×10^4 . IGO TFTs may act as photodetectors according to the results obtained for optical properties.

Keywords: thin-film transistor; oxygen vacancies; co-sputtering

1. Introduction

Amorphous oxide semiconductor thin-film transistors (TFTs) have been widely applied to flat-panel displays, personal digital assistant computers, and smart phones [1]. These transistors are attractive materials as they exhibit electrical characteristics that are superior to those of conventional amorphous silicon TFTs; these characteristics include high carrier mobility, high stability, transparency, and a low-temperature processing requirement [2,3]. Indium oxide (In₂O₃)-based binary compounds are excellent materials for TFT devices. These materials are transparent and feature a wide bandgap (~3.2 eV), high electrical conductivity, and optical transparency owing to the native oxygen vacancies that act as donors and indium interstitials. Hence, In₂O₃ can act as carrier in multicomponent oxide material systems [4]. In₂O₃-based TFTs, as wide bandgap materials, combine electrical and optical functions for photonic integrated circuits, which can serve as photodetectors. Bandgap energy can be tuned by doping other materials, which could be classified as visible-blind photodetectors

($\lambda \leq 400$ nm) and solar-blind photodetectors ($\lambda \leq 280$ nm), although the process depends on the cutoff wavelength [5,6].

Among transistor materials, gallium oxide (Ga_2O_3) is one of the promising active layers. Ga_2O_3 is a wide-bandgap semiconductor with ~ 4.9 eV; it is an optically transparent material and features poor conductivity [7]. Therefore, Ga_2O_3 is the most commonly used component in electronic devices, such as ultraviolet (UV) photodetectors, power electronic devices, light-emitting diodes, and transparent conducting films [8–11]. However, Ga is a carrier suppressor, which reduces oxygen vacancy in control carrier concentrations in multicomponent oxide TFT devices. The poor conductivity of Ga_2O_3 offsets the material's electrical characteristics. Therefore, doping with indium is often used for effectively improving electrical conductivity [12]. The bond strength of Ga–O is higher than that of In–O, which serves as a carrier that suppresses and improves the stability of components [13].

Oxygen vacancies are crystal defects that play a central role in metal oxides and act as donors to provide charge carriers. The components can be optimized by varying the defects [14]. Influencing oxygen vacancy defects through sputtering has been reported by various studies, wherein growth pressure and oxygen flow rate were modulated, and defect concentration and device performance were improved by doping different materials [15–17], which can be used in a wide range of applications due to their high deposition rate, easy deposition to metals, alloys, and compounds, enabled control of film composition, high purity, and low cost [18]. Meanwhile, flame detection, oil spill detection, UV astronomy, and semiconductor lithography require UV detection, which can be achieved by using wide-bandgap semiconductors, which are highly transparent and inexpensive and require low-temperature processes [19]. Hence, wide-bandgap semiconductors can be used not only as channel layers for TFT but also as ideal photodetectors [20]. We fabricated indium gallium oxide (IGO) TFTs by using the co-sputtering method, which integrates photodetectors and TFT in measuring the optical and electrical properties of a device and in which measurements depend on the different deposition power requirements of In_2O_3 targets. The effects of oxygen vacancies on the characteristics of photodetectors were determined by analyzing thin-film properties using X-ray photoelectron spectroscopy (XPS).

2. Device Fabrication and Characterization

Figure 1 shows a schematic of the p-type bottom gate IGO TFT structure used in this study. The 300 nm-thick SiO_2 dielectric layer was grown on a heavily doped p-type silicon through wet oxidation. Then, the patterned IGO thin film was deposited on the SiO_2 layer with shadow mask using a radiofrequency (RF) magnetron co-sputtering system (AST, Tainan, Taiwan) at room temperature. The RF powers applied to Ga_2O_3 were fixed at 100 W, and the In_2O_3 power was set to 50, 60, or 70 W. Argon flow was fixed at 3 sccm under a gas pressure of 5 mTorr and base pressure of approximately 3×10^{-5} Torr. For convenience, the RF power condition ($\text{Ga}_2\text{O}_3/\text{In}_2\text{O}_3$) was set to 100 W/50 W, 100 W/60 W, and 100 W/70 W for samples A, B, and C, respectively. After deposition, the IGO thin films were annealed in an argon environment at 300 °C for 1 h. Finally, the 100 nm patterned Al source and drain electrode were deposited by thermal evaporation. The channel length (L) and width (W) were 100 and 1000 μm , respectively. The thin-film properties were measured by X-ray diffraction (XRD, D8 Discover, Bruker, Billerica, MA, USA), XPS (PHI 5000 VersaProbe, ULVAC, Chigasaki-shi, Japan), atomic force microscopy (AFM, Solver P47, NT-MDT, Moscow, Russia), and UV-visible spectroscopy (U4100, HITACHI, Tokyo, Japan). The electrical characteristics were measured by Agilent B1500 semiconductor device analyzer (Agilent Technologies, Santa Clara, CA, USA) at room temperature and in the dark. The optical properties were measured by Jobin Yvon SPEX system (Kyoto, Japan) with a 150-W Xe arc lamp light source.

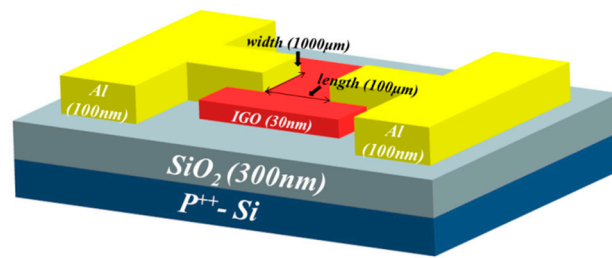


Figure 1. Schematic of IGO TFTs.

3. Results and Discussion

Figure 2 shows the XRD data of samples A, B, and C. Results showed that no peak was relevant to the three samples, indicating that the samples were in an amorphous phase.

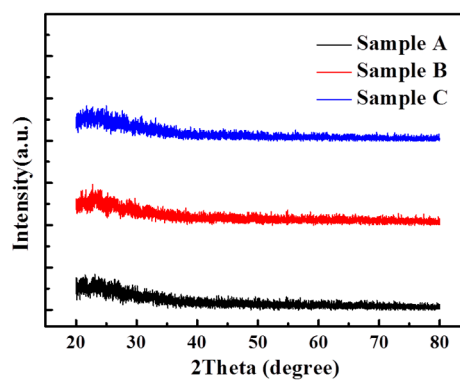


Figure 2. XRD spectra of three IGO thin-film samples exhibited no peak, indicating that all samples were in an amorphous phase.

The AFM images in Figure 3 show that the root mean square of the insulator layer measured 1.0147 nm. The smooth surface positively influenced the electrical properties and stability; such a condition could avoid electron trapping at the insulator-channel interface [21]. Meanwhile, we performed AFM measurements for samples A, B, and C, shown in Figure 4. The root mean square (Rq) values were 1.207, 1.249, and 1.54 for sample A, B, and C, respectively. The increased roughness could be due to the high deposition rate, which increased along with the deposition power.

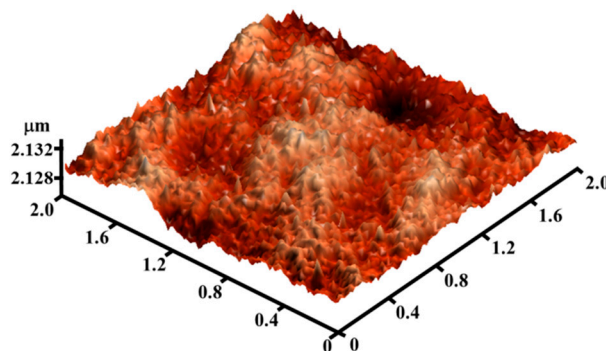


Figure 3. AFM images of dielectric layer exhibiting a smooth surface that could avoid electron trapping at the insulator-channel interface.

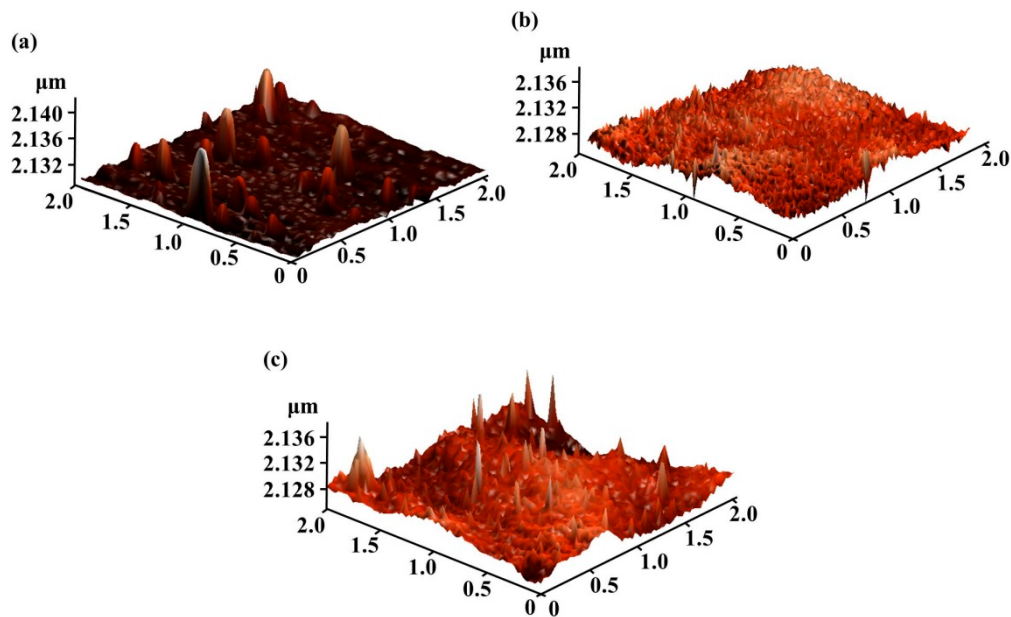


Figure 4. AFM image with RF deposition power of (a) sample A: 50W (b) sample B: 60W (c) sample C: 70W. The Rq values reached 1.207, 1.249, and 1.54, respectively.

Figure 5 shows the transfer characteristics of IGO TFT for samples A, B and C. Table 1 presents the electrical performance of the threshold voltage (V_{th}), on-off current ratio (I_{on}/I_{off}), subthreshold swing (S.S), and field-effect mobility. The I_{DS} and V_{GS} curves were measured from -6 V to 10 V, and V_{DS} was fixed at 6 V. Field-effect mobility and S.S can be extracted using the following equations:

$$I_{DS} = \frac{\mu C_{OX} W}{2L} (V_{GS} - V_{th})^2, \quad (1)$$

$$S = \frac{\partial V_G}{\partial(\log I_D)}, \quad (2)$$

where C refers to the capacitance of dielectric layer, V_{th} denotes the threshold voltage, W and L are the channel width and length, respectively. With the increase in indium content, the field-effect mobility increased, and V_{th} exhibited a negative shift as the increased oxygen vacancy concentration increased the carrier concentration. Moreover, the excess oxygen vacancies, which cause an off current, were unsuppressed because of the increase in conductivity of the IGO layer. Carrier concentration was generated by oxygen vacancy formation, and gallium suppressed oxygen vacancy formation owing to the high bond strength between In and O. Thus, when the deposition power of In_2O_3 targets increased, the S.S characteristics deteriorated [22]. The optimum performance of IGO TFTs was observed in sample B, which yielded a V_{th} of 1.1 V, S.S of 3.82 V/dec, field-effect mobility of 1.45 cm^2/Vs , and an I_{on}/I_{off} ratio of 4.5×10^6 . Figure 6 shows the output characteristics of samples A, B, and C. The I_{DS} and V_{DS} curves ranged from 0 V to 10 V, and $V_{GS} = 0$ V– 10 V in six steps. The output characteristic curves expressed clear pinch off voltage and current saturation. The saturation drain current was approximately 3.18×10^{-7} , 7.87×10^{-6} , and 1.35×10^{-5} A at $V_{GS} = 10$ V for samples A, B, and C, respectively.

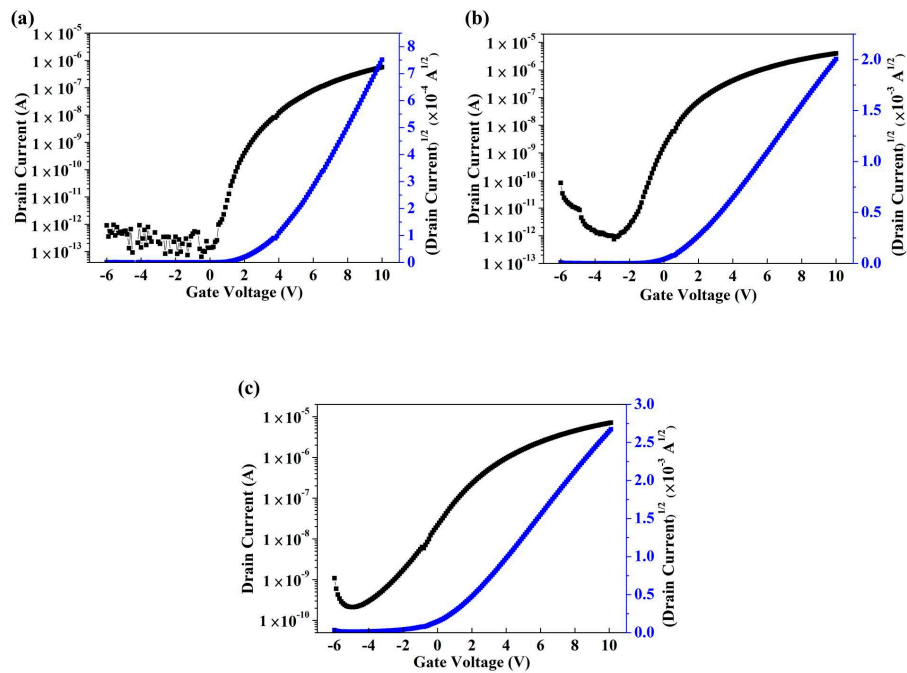


Figure 5. Transfer characteristics of IGO TFTs with different deposition powers of In_2O_3 . (a) Sample A: 50 W, (b) sample B: 60 W, and (c) sample C: 70 W.

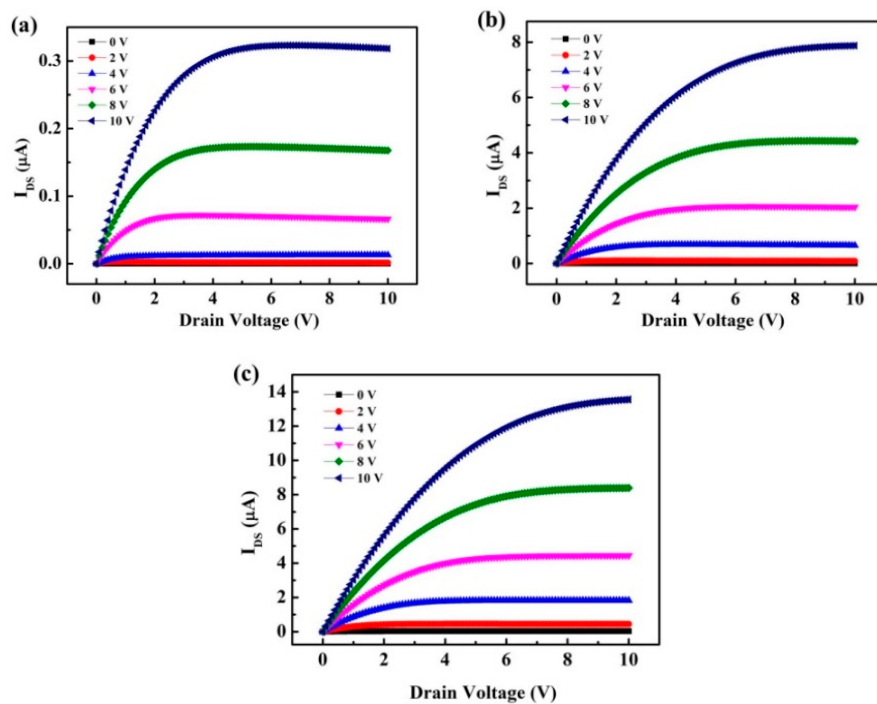


Figure 6. Output characteristics of IGO TFTs with different deposition power of In_2O_3 . (a) Sample A: 50 W, (b) sample B: 60 W, and (c) sample C: 70 W.

Table 1. Electrical performance parameters of IGO TFTs at different deposition power of In_2O_3 target.

	$I_{\text{on}}/I_{\text{off}}$ Ratio	S.S (V/dec)	μ_{FE} (cm^2/Vs)	V_{TH} (V)
Sample A	4.3×10^5	0.526	0.4	3.7
Sample B	4.5×10^6	3.82	1.45	1.1
Sample C	4×10^4	8.3	2.26	0.6

Figure 7 shows the XPS measurement results, indicating that the O1s XPS spectra of samples A, B, and C feature different deposition powers of In_2O_3 target. The O1s spectra were decomposed by Gaussian fitting, which resolved two peaks. The first peak was located at approximately 530 ± 0.2 eV, which is generally attributed to the atomic oxygen of the IGO thin film. The second peak was located at approximately 531.6 eV, which is associated with oxygen vacancies in the IGO thin film. The XPS results indicate that the ratios of oxygen vacancies reached 46.34%, 50.3%, and 56.3% for samples A, B, and C, respectively. These values show that an increase in sputtering power for In_2O_3 resulted in higher amounts of oxygen vacancies, that is, from 46% to 56%. Oxygen was easily released because of the low strength of In–O bonds. This finding indicates that In_2O_3 content increased as oxygen vacancies increased from 46% to 56%. Oxygen vacancies dominate the conductivity of semiconductors and increase electron concentrations. Thus, oxygen vacancies can act as charge carriers in IGO thin films. Conductivity was improved by increasing the In_2O_3 content, thereby indicating the mobility enhancement of IGO TFTs.

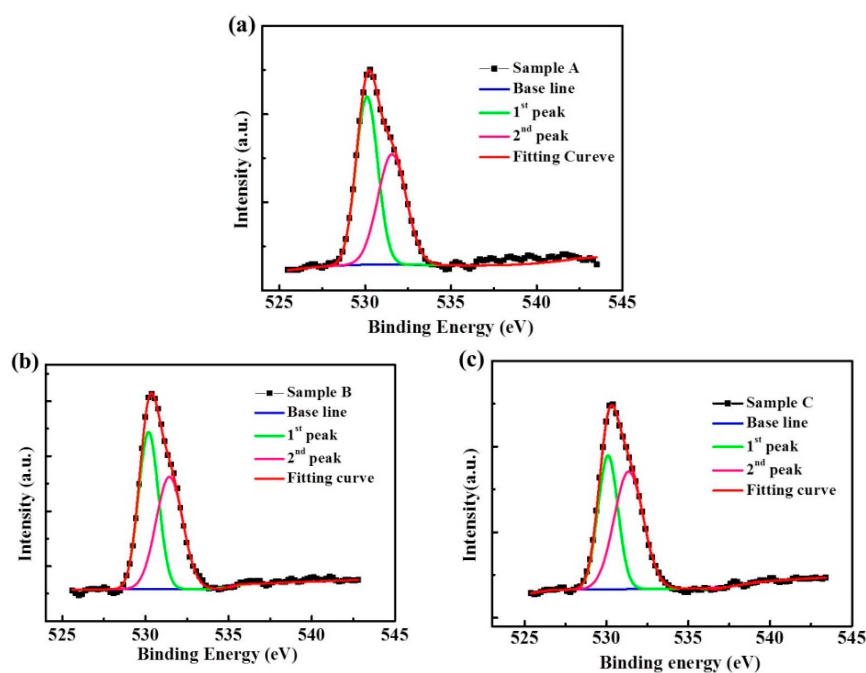


Figure 7. O1s XPS spectra of (a) samples A, (b) sample B, and (c) sample C under various sputtering power.

Figure 8a shows the transfer characteristics of IGO TFTs under the dark region and UV illumination. Considering that sample B exhibits optimal characteristics due to excessive large number of carriers, sample C featured a larger off current. Hence, the lower $I_{\text{on}}/I_{\text{off}}$ current ratio was 4×10^4 ; the $I_{\text{on}}/I_{\text{off}}$ current reflects the capacity switching to TFT. On the other hand, a small S.S represents the response speed of TFTs, which require achieving a quick switch behavior. According to the above findings, we defined sample B as the best performing sample. The device was measured under dark condition and under UV illumination from 400 nm to 300 nm. The I_{DS} and V_{GS} curves indicate that the current response of the IGO phototransistor increased after illumination due to photo-generated carrier injection in the channel IGO layer.

Figure 8b presents the use of a xenon lamp exposure for IGO TFTs, where the responsivity of the device ranged from 500 nm to 250 nm under $V_{\text{GS}} = -5$ V and $V_{\text{DS}} = 6$ V. Figure 8c shows the optical bandgap of sample B, and it could be calculated from the Tauc plot expressed as follows:

$$\alpha h\nu = (h\nu - E_g), \quad (3)$$

where α denotes the absorption coefficient, $h\nu$ refers to the photo energy, and E_g represents the energy bandgap. Linear fitting of the absorption spectra of sample B was approximately 4 eV for indirect transition, and the cutoff wavelength was approximately 310 nm. In this regard, responsivity could be obtained using the following equation:

$$R = \frac{I_{ph}}{P_{opt}}, \quad (4)$$

where I_{ph} stands for the output current, and P_{opt} indicates the optical power. The responsivity of the device measured 0.16 A/W, and the UV-to-visible rejection ratio reached 8×10^4 . The UV-to-visible rejection ratio was defined as responsivity and measured at 300 nm and divided by the responsivity measured at 450 nm. The highest UV-to-visible rejection ratio signifies that the device was sensitive to UV light. The IGO TFTs show extreme promise as UV photodetectors. Figure 8d shows the dynamic responses of sample B under UV illumination at 300 nm with $V_G = -5$ V and $V_D = 6$ V. The current rapidly increased under illumination and decreased when the light was turned off. The responses measured from sample B were stable and reproducible. The rise time was 24.11 s, and decay time was 21.39 s. In this work, oxygen vacancy concentration changed by In doping, with increased oxygen vacancies leading to improved electric properties of IGO TFTs. as well as, the photo properties show the IGO TFTs have a potential can be used for a UV photodetector applied on flame detection or oil spill detection.

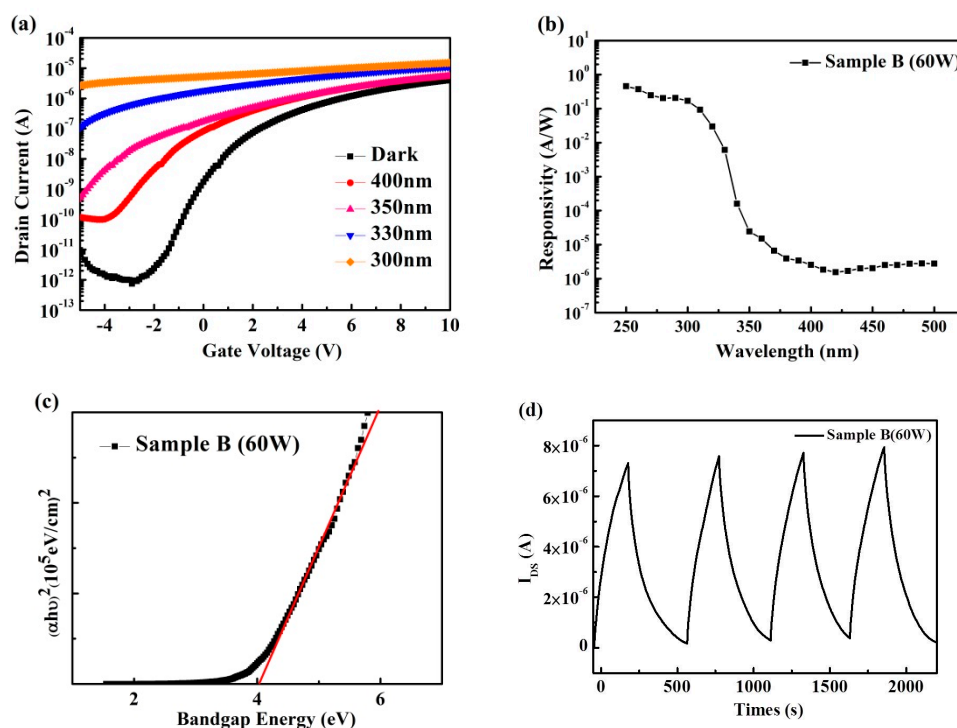


Figure 8. (a) Transfer characteristics of IGO TFTs under THE dark region and UV illumination from 400 nm to 300 nm with a V_G function from -6 V to 10 V and fixed V_{DS} at 6 V. (b) Responsivity of sample B measured in the 350–500 nm wavelength. (c) Indirect bandgap values of sample B using Tauc plots and linear fitting. (d) Dynamic responses of sample B under UV illumination at 300 nm and with $V_G = -5$ V and $V_D = 6$ V.

4. Conclusions

In summary, we reported the fabrication of IGO TFTs with different deposition power of In_2O_3 target by co-sputtering deposition. The device performance could modulate the content of In_2O_3 . The oxygen vacancies represented the majority of charge carriers. The number of oxygen vacancies increased with the deposition power of the In_2O_3 target. The best device performance was obtained

at a deposition power of 60 W (sample B), exhibiting a V_{th} of 1.1 V, I_{on}/I_{off} current ratio of 4.5×10^6 , field-effect mobility of $1.42 \text{ cm}^2/\text{Vs}$, and S.S of $3.82 \text{ V}/\text{dec}$. IGO TFTs can also be used in UV detection. The responsivity of the device was $0.16 \text{ A}/\text{W}$, and the UV-to-visible rejection ratio can reach 8×10^4 , indicating that the IGO TFTs act as UV photodetectors.

Author Contributions: K.-Y.C. and C.-C.Y. wrote the manuscript; K.-Y.C. and C.-C.Y. performed the experiments; K.-Y.C., C.-C.Y., and Z.-H.W. analyzed the data; C.-C.Y., H.-C.Y. and Y.-K.S. reviewed the manuscript.

Funding: This research was supported by the Ministry of Science and Technology of Taiwan, ROC under Contract No. MOST 104-2221-E-168-011-MY3 and 107-2221-E-006-185-MY3 and the Green Energy Technology Research Center, Department of Electrical Engineering, Kun Shan University, Tainan, Taiwan.

Conflicts of Interest: The authors declare no conflict of interest.

References

1. Kumomi, H.; Kamiya, T.; Hosono, H. Advances in oxide thin-film transistors in recent decade and their future. *ECS Trans.* **2015**, *67*, 3–8. [[CrossRef](#)]
2. Nomura, K.; Ohta, H.; Takagi, A.; Kamiya, T.; Hirano, M.; Hosono, H. Room-temperature fabrication of transparent flexible thin-film transistors using amorphous oxide semiconductors. *Nature* **2004**, *432*, 488–492. [[CrossRef](#)] [[PubMed](#)]
3. Choi, C.-H.; Han, S.-Y.; Su, Y.-W.; Fang, Z.; Lin, L.-Y.; Cheng, C.-C.; Chang, C.-H. Fabrication of high-performance, low-temperature solution processed amorphous indium oxide thin-film transistors using a volatile nitrate precursor. *J. Mater. Chem. C* **2015**, *3*, 854–860. [[CrossRef](#)]
4. Korotcenkov, G.; Brinzari, V.; Cho, B.K. In_2O_3 -based multicomponent metal oxide films and their prospects for thermoelectric applications. *Solid State Sci.* **2016**, *52*, 141–148. [[CrossRef](#)]
5. Sang, L.; Liao, M.; Sumiya, M. A comprehensive review of semiconductor ultraviolet photodetectors: From thin film to one-dimensional nanostructures. *Sensors* **2013**, *13*, 10482–10518. [[CrossRef](#)] [[PubMed](#)]
6. Armstrong, A.M.; Klein, B.; Allerman, A.A.; Douglas, E.A.; Baca, A.G.; Crawford, M.H.; Pickrell, G.W.; Sanchez, C.A. Visible-blind and solar-blind detection induced by defects in ALGaN high electron mobility transistors. *J. Appl. Phys.* **2018**, *123*, 114502. [[CrossRef](#)]
7. Orita, M.; Ohta, H.; Hirano, M.; Hosono, H. Deep-ultraviolet transparent conductive $\beta\text{-Ga}_2\text{O}_3$ thin films. *Appl. Phys. Lett.* **2000**, *77*, 4166–4168. [[CrossRef](#)]
8. Guo, D.Y.; Wu, Z.P.; An, Y.H.; Guo, X.C.; Chu, X.L.; Sun, C.L.; Li, L.H.; Li, P.G.; Tang, W.H. Oxygen vacancy tuned ohmic-schottky conversion for enhanced performance in $\beta\text{-Ga}_2\text{O}_3$ solar-blind ultraviolet photodetectors. *Appl. Phys. Lett.* **2014**, *105*, 023507. [[CrossRef](#)]
9. Higashiwaki, M.; Sasaki, K.; Murakami, H.; Kumagai, Y.; Koukitu, A.; Kuramata, A.; Masui, T.; Yamakoshi, S. Recent progress in Ga_2O_3 power devices. *Semicond. Sci. Technol.* **2016**, *31*, 034001. [[CrossRef](#)]
10. Stanish, P.C.; Radovanovic, P.V. Energy transfer between conjugated colloidal Ga_2O_3 and CdSe/CdS core/shell nanocrystals for white light emitting applications. *Nanomaterials* **2016**, *6*, 32. [[CrossRef](#)] [[PubMed](#)]
11. Wang, H.; Zhou, Q.; Liang, S.; Wen, R. Fabrication and characterization of ALGaN-based UV LEDs with a $\text{ITO}/\text{Ga}_2\text{O}_3/\text{Ag}/\text{Ga}_2\text{O}_3$ transparent conductive electrode. *Nanomaterials* **2019**, *9*, 66. [[CrossRef](#)] [[PubMed](#)]
12. Parthiban, S.; Kwon, J.-Y. Role of dopants as a carrier suppressor and strong oxygen binder in amorphous indium-oxide-based field effect transistor. *J. Mater. Res.* **2014**, *29*, 1585–1596. [[CrossRef](#)]
13. Nomura, K.; Takagi, A.; Kamiya, T.; Ohta, H.; Hirano, M.; Hosono, H. Amorphous oxide semiconductors for high-performance flexible thin-film transistors. *Jpn. J. Appl. Phys.* **2006**, *45*, 4303–4308. [[CrossRef](#)]
14. Pacchioni, G. Oxygen vacancy: The invisible agent on oxide surfaces. *Chemphyschem* **2003**, *4*, 1041–1047. [[CrossRef](#)] [[PubMed](#)]
15. Reddy, Y.A.K.; Shin, Y.B.; Kang, I.-K.; Lee, H.C. Effect of sputtering pressure on microstructure and bolometric properties of $\text{Nb}:\text{TiO}_{2-x}$ films for infrared image sensor applications. *J. Appl. Phys.* **2016**, *119*, 044504. [[CrossRef](#)]
16. Chen, K.-Y.; Hsu, C.-C.; Yu, H.-C.; Peng, Y.-M.; Yang, C.-C.; Su, Y.-K. The effect of oxygen vacancy concentration on indium gallium oxide solar blind photodetector. *IEEE Trans. Electron Devices* **2018**, *65*, 1817–1822. [[CrossRef](#)]

17. Li, S.-S.; Su, Y.-K. Oxygen-vacancy induced resistive switching effect in mn-doped zno memory devices. *Phys. Status Solidi (RRL)-Rapid Res. Lett.* **2018**, *13*, 1800453. [[CrossRef](#)]
18. Swann, S. Magnetron sputtering. *Phys. Technol* **1988**, *19*, 67. [[CrossRef](#)]
19. Zou, Y.; Zhang, Y.; Hu, Y.; Gu, H. Ultraviolet detectors based on wide bandgap semiconductor nanowire: A review. *Sensors* **2018**, *18*, 2072. [[CrossRef](#)] [[PubMed](#)]
20. Ivanoff Reyes, P.; Ku, C.-J.; Duan, Z.; Xu, Y.; Garfunkel, E.; Lu, Y. Reduction of persistent photoconductivity in ZnO thin film transistor-based UV photodetector. *Appl. Phys. Lett.* **2012**, *101*, 031118. [[CrossRef](#)]
21. Zhou, S.; Fang, Z.; Ning, H.; Cai, W.; Zhu, Z.; Wei, J.; Lu, X.; Yuan, W.; Yao, R.; Peng, J. Bias stability enhancement in thin-film transistor with a solution-processed ZrO₂ dielectric as gate insulator. *Appl. Sci.* **2018**, *8*, 806. [[CrossRef](#)]
22. Jun, T.; Song, K.; Jung, Y.; Jeong, S.; Moon, J. Bias stress stable aqueous solution derived y-doped ZnO thin film transistors. *J. Mater. Chem.* **2011**, *21*, 13524–13529. [[CrossRef](#)]



© 2019 by the authors. Licensee MDPI, Basel, Switzerland. This article is an open access article distributed under the terms and conditions of the Creative Commons Attribution (CC BY) license (<http://creativecommons.org/licenses/by/4.0/>).